RESEARCH ARTICLE

NANO · MICRO small
www.small-journal.com

Bioinspired Omnidirectional Iontronic Sensors Based on Triboelectric Charge

Zunkang Zhou, Yan Du, Yuyang Zhang, Jie Fu, Yaowen Ouyang, Zhong Lin Wang, and Di Wei**

Flexible pressure sensors are critical components in next-generation wearable electronics and intelligent human-machine interface (HMI). However, conventional designs often suffer from limited sensitivity and uniaxial force detection, restricting their applicability in complex environments. Here, a bioinspired omnidirectional iontronic sensor (BOIS) is presented, engineered via triboelectric coupling and featuring a cross-scale architecture inspired by the spatial encoding properties of cochlear cilia. Through the integration of a 70° inclined macroscopic ciliary array based on Fibonacci helix optimization and 3D printing technology, the sensor achieves high-resolution detection of both normal and shear forces. The incorporation of iontronic effects further enhances sensitivity via synergistic charge modulation. The resulting flexible sensing platform demonstrates excellent mechanical compliance, multi-axis responsiveness, and high precision in monitoring dynamic joint motions such as wrist bending and finger flexion. This work offers a robust strategy for advancing omnidirectional tactile sensing, with promising applications in medical rehabilitation, soft robotics, and HMI.

1. Introduction

Pressure/haptic sensors, as core components for converting mechanical stress into electrical signals, have played an increasingly important role in areas such as intelligent robotics, wearable devices, and smart healthcare.[1–5] In recent years, with the advancement of materials science and micro and nano fabrication technologies, various types of pressure sensors based on different electromechanical transduction mechanisms such as piezoresistive,[6–8] capacitive,[9–11] and piezoelectric[12–14] have been developed. These sensors have achieved significant improvements in performance, promoting their application in flexible electronics and human-machine interface (HMI). Despite these advances, conventional pressure sensors continue to encounter fundamental limitations in meeting the demands of next-generation intelligent systems. Piezoresistive sensors are susceptible to signal drift and nonlinearity under repeated loading; capacitive sensors are vulnerable to environmental disturbances, including parasitic capacitance and electromagnetic interference; and piezoelectric sensors, while effective for dynamic sensing, perform poorly in quasi-static pressure detection.[15–17] In addition, the performance of these sensors is often highly dependent on complex external circuitry, high-precision signal conditioning modules, or rigid substrates, which imposes challenges for integration into flexible, miniaturized, and self-sustainable platforms. These constraints highlight the need for novel transduction mechanisms that are not only sensitive and adaptable, but also structurally simple, mechanically compliant, and energy autonomous.

Among the various electromechanical transduction mechanisms, the triboelectric nanogenerator (TENG) has emerged as a highly promising strategy for developing next-generation pressure sensors due to its unique energy conversion principle and material versatility.[18–22] Ideally, a pressure sensor should integrate high sensitivity with a wide detection range, as the surface charge density is the key factor determining the sensitivity of triboelectric devices. The performance optimization of such sensors primarily hinges on the morphological architecture design of the active layer.[23] A diverse array of surface and internal microstructures, such as hemispheres,[24,25] needles,[26,27] columns,[28,29] cones,[30–32] wrinkles,[33,34] and porous structures,[35,36] have been engineered to serve as dielectric layers. However, most existing designs are limited to responding to a single physical parameter or stimulus

Z. Zhou, Y. Du, Y. Ouyang, Z. L. Wang, D. Wei
Beijing Institute of Nanoenergy and Nanosystems
Chinese Academy of Sciences
Beijing 101400, China
E-mail: zlwang@binn.cas.cn; weidi@binn.cas.cn
Z. Zhou, Y. Du, Y. Ouyang
School of Nanoscience and Engineering
University of Chinese Academy of Sciences
Beijing 100049, China
Y. Zhang
The University of Manchester
Manchester M13 9PL, UK
J. Fu
ZHEJIANG WANSHENG CO., LTD.
Zhejiang, China
D. Wei
Centre for Photonic Devices and Sensors
University of Cambridge
9 JJ Thomson Avenue, Cambridge CB3 0FA, UK

The ORCID identification number(s) for the author(s) of this article can be found under https://doi.org/10.1002/smll.202510157

DOI: 10.1002/smll.202510157

in a unidirectional manner, which hinders the realization of omnidirectional sensing. Therefore, the development of new structural designs that can achieve omnidirectional response, and even non-contact detection has become a crucial direction for the next-generation of intelligent sensing technologies. In this context, biologically inspired architectures offer a compelling pathway toward achieving enhanced sensing functionality and system adaptability. In the human cochlea, ciliary structures exhibit remarkable sensitivity to subtle basilar membrane vibrations, enabling precise auditory perception.[37,38] Rather than adopting a fixed orientation, cochlear cilia display a directionally selective, dynamic distribution, significantly enhancing multidirectional and frequency-specific signal detection. Nature offers numerous paradigms of omnidirectional perception and structural optimization, among which the Fibonacci spiral, rooted in the golden ratio, stands out as a hallmark of efficiency and adaptability.[39] For example, plants modulate auxin distribution to position leaves and branches at golden angles, forming self-similar Fibonacci spirals that optimize spatial utilization and maximize exposure to environmental stimuli such as sunlight.[40] Inspired by these biologically optimized architectures, we designed a TENG-based pressure sensor that incorporates a Fibonacci-guided structural layout to achieve adaptive, omnidirectional response. This bioinspired strategy represents a key advancement toward next-generation intelligent tactile sensing.

Beyond structural optimization, recent progress in interfacial charge engineering has opened new avenues for enhancing the sensitivity and functionality of triboelectric sensors. Notably, the recent development of triboiontronics has further extended the potential of TENGs in intelligent sensing applications.[41–43] Li et al. dynamically modulated the electrical double layer (EDL) structure through contact electrochemistry (CE), realizing a highly efficient triboiontronics system for energy and information flow. This approach establishes a new paradigm for energy harvesting and neuromorphic computing.[44] By coupling triboelectric effects with ionic or electronic transport phenomena, especially through the introduction of electrolyte environments at material interfaces to form EDL, this approach significantly enhances signal conversion sensitivity and response performance.[45] The EDL, as a highly localized charge accumulation mechanism, enables rapid response to minute mechanical disturbances, thereby greatly improving the detection of low frequency and small amplitude pressure signals and increasing the dynamic response speed and resolution of the system. Building on this foundation, the synergistic interaction between triboelectric and EDL effects not only optimizes the sensor's ability to detect subtle pressure and dynamic contact events, but also allows for multifunctional integration, including the sensitive detection of shear forces, vibrations. This advancement lays a solid technical foundation and offers broad prospects for the development of next-generation intelligent pressure sensing systems with high resolution and multimodal responsiveness.

Polydimethylsiloxane (PDMS) plays a central role in BOIS devices due to its outstanding physicochemical properties, excellent biocompatibility, and high compatibility with microstructural designs.[46,47] Its low surface energy, high elastic deformation capability, and biological safety enable it to adapt to complex operating environments while ensuring the mechanical durability of devices, making it highly suitable for wearable health monitoring sensors. For instance, Zhang et al. developed a multimodal sensing platform integrating a mechanically color-changing Fe_3O_4-carbon nanoparticle layer, a thermosensitive ionic hydrogel layer, and a triboelectric carbon nanotube/PDMS electrode layer. It achieved sensitivities of −528.0 and −63.7 V kPa^{-1} in the 0–2 kPa and 2–9 kPa pressure ranges, respectively, with a detection limit of 65 Pa.[48] Kim et al. constructed a self-powered dual-electrode sensor using PDMS sponge and polyacrylamide (PAAM) hydrogel to encapsulate the electrolyte. This sensor exhibits a sensitivity of 10 V kPa^{-1} and a detection range up to 110 kPa, demonstrating excellent stability and environmental adaptability. These studies fully demonstrate the critical value of PDMS in constructing high-performance, durable flexible sensing systems.[49]

Herein, we present a bioinspired omnidirectional iontronic sensor (BOIS) based on triboelectric coupling, enabled by a cross-scale structural design with Fibonacci spiral optimization strategy. The sensor features self-powered detection of normal and shear forces, addressing the persistent challenge of unidimensional sensing in conventional pressure sensors. Drawing inspiration from the spatial encoding of cochlear basilar membrane cilia, inclined macroscopic ciliary array was fabricated on PDMS dielectric layers via 3D printing. The Fibonacci spiral optimization algorithm generates a 70° tilt structure,[50] which is within the natural inclination range of the cochlear basilar membrane cilia. This bio-inspired alignment enhances directional sensitivity in omnidirectional sensors. A 70° tilt angle was identified as optimal for sensing performance through contact-separation tests, aligning well with theoretical predictions. COMSOL simulations further revealed the role of geometric configuration in governing angle-dependent electrical output via electromechanical coupling. To enhance pressure sensitivity, the iontronic effect was integrated into a hydrogel configuration, where dynamic modulation of the EDL at the hydroxyethyl acrylate (HEA) hydrogel/PDMS interface induced capacitance changes and alternating current signals. Asymmetric contact generated uneven interfacial charge distribution, significantly improving sensitivity to subtle mechanical stimuli. The inclined macroscopic ciliary array demonstrated excellent linearity and enhanced second-order sensitivity compared to planar architectures, attributed to stress-gradient amplification from the bioinspired structure. With high flexibility, sensitivity, and omnidirectional sensing capability, the BOIS system achieved accurate monitoring of complex human motions including finger flexion, wrist bending, and knee articulation. These results underscore its potential in medical rehabilitation, wearable electronics, intelligent interfaces, and biomechanical diagnostics.

2. Results and Discussion

2.1. Ciliated Surface Structural Design

Inspired by the spatial encoding mechanism of cochlear hair cells in detecting multilevel acoustic vibrations, we developed a BOI featuring a 70° inclined macroscopic ciliary array architecture optimized via the golden angle principle (**Figure 1a**). The Fibonacci spiral generates a 70° inclined structure (Figure S1, Supporting Information), a geometrically favorable angle that maximizes spatial distribution and minimizes overlap in arrayed elements. Interestingly, this 70° inclination falls within the natural

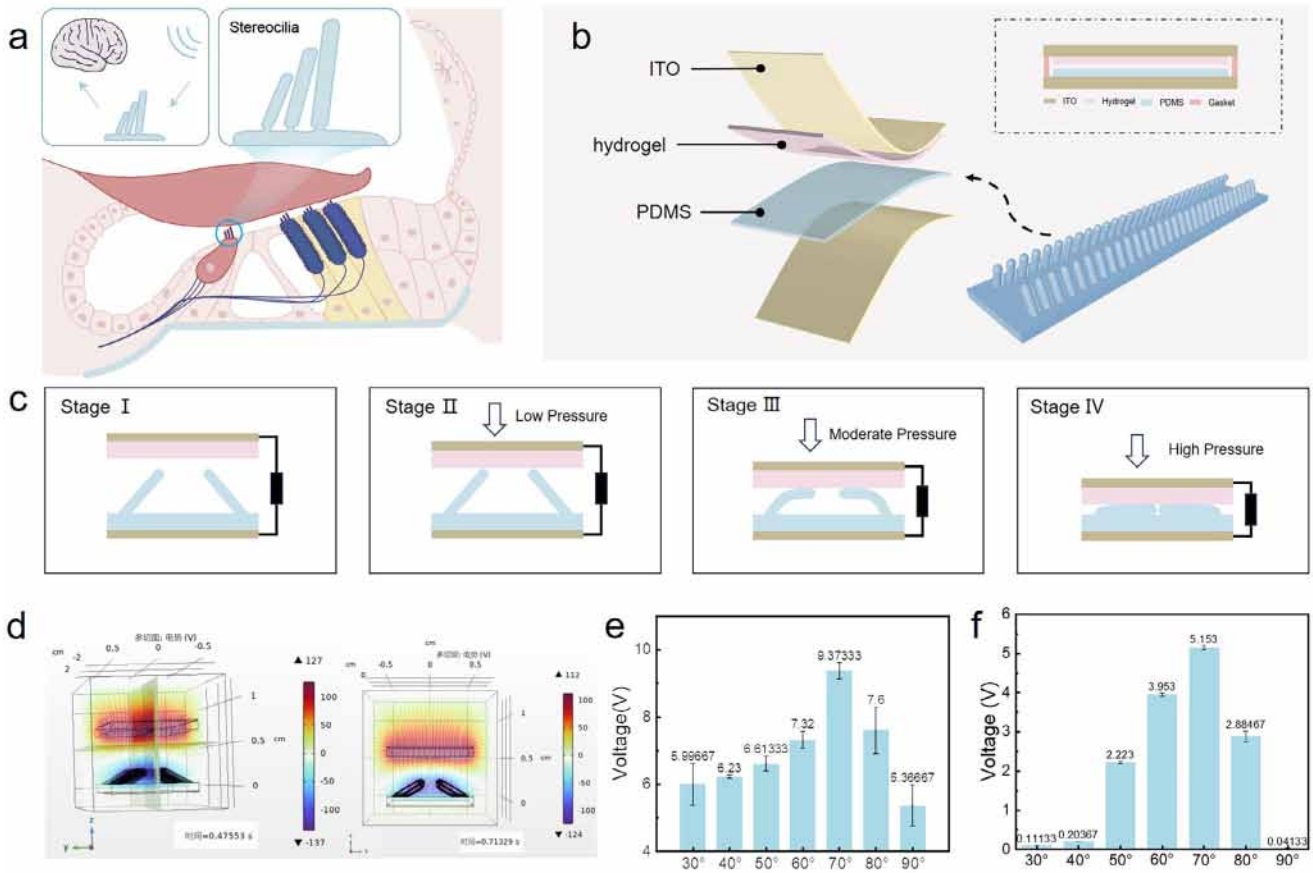

Figure 1. Design and simulation analysis of bioinspired omnidirectional iontronic sensor based on bionics of cochlear cilia. a) Schematic diagram of the gradient distribution of inner and outer hair cells in the cochlear Corti organ, the structure of cochlear cilia, and the mechanism of sound perception. b) Schematic diagram of multilayer heterogeneous structure of BOIS based on contact-separation mode. c) Schematic diagram of the deformation cross-section of the inclined macroscopic cilia array of BOIS under different pressure gradients. d) COMSOL simulation analysis of the potential distribution during the contact separation process of nylon-PDMS. e) Comparison chart of the output of nylon and PDMS inclined macroscopic ciliary array at different tilt angles. f) Comparison images of HEA hydrogel and PDMS ciliary array outputs at different tilt angles.

inclination range of cilia bundles in the basilar membrane of the cochlear, which are specifically designed to capture multidirectional acoustic signals with high spatial resolution. Inspired by this biological principle, we adopted a 70° inclined macroscopic ciliary array in our BOIS design to enable enhanced omnidirectional mechanical sensing. Comparative analysis with other tilt angles confirmed that the 70° configuration provides superior signal anisotropy and spatial responsiveness. To fabricate this architecture, a sacrificial templating strategy was adopted to ensure high geometric fidelity and scalable processing. A custom-designed negative mold incorporating 70° inclined channels was fabricated using high-resolution stereolithography 3D printing, with polyvinyl alcohol (PVA) serving as the sacrificial material. The PDMS precursor was cast into the mold, degassed, and thermally cured at 60 °C to form a flexible elastomeric matrix. Subsequent immersion in deionized water selectively dissolved the embedded PVA, yielding a freestanding PDMS membrane with uniformly aligned, inclined macroscopic ciliary array. This approach eliminates the need for complex etching or solvent-based template removal, while the one-step molding process ensures consistent microstructural replication. As demonstrated in Figure S2 (Supporting Information), this method enables precise realization of bioinspired architectures and offers a robust foundation for the development of high-performance iontronic sensing platforms.

As illustrated in Figure 1b, the BOIS was composed of a multilayered architecture, where indium tin oxide (ITO) films, commercially available, were deposited in advance onto polyethylene terephthalate (PET) substrates via radiofrequency (RF) magnetron sputtering. ITO was chosen for its high optical transparency, low sheet resistance, and mechanical flexibility, making it a reliable flexible electrode material for transparent and deformable sensing systems. The triboelectric interface consisted of HEA hydrogel as the tribopositive material and PDMS as the tribonegative dielectric layer. PDMS was chosen for its low electron affinity, excellent elasticity, biocompatibility, and chemical stability, making it particularly suitable for deformable triboelectric sensing components. Remarkably, oxygen plasma treatment was employed to activate interfacial surfaces, enabling covalent bonding between heterogeneous material layers and significantly enhancing interfacial stability during dynamic deformation. Under external mechanical loading, the device drove the HEA hydrogel and PDMS dielectric layers into periodic contact-separation cycles. Charge transfer occurred at the interface due to

differences in electron affinity between the dielectric materials, generating an EDL effect. During separation, electrostatic induction generated electrical signals between the ITO electrodes.

The sensitivity of this BOIS originated from the dynamic reconstruction mechanism of the EDL induced by the deformation of the inclined macroscopic ciliary array under pressure gradients, and its operational process could be divided into four characteristic stages (Figure 1c): In Stage I, the tribopositive/tribonegative dielectric layers were isolated by spacers to form a quasi-static EDL; upon pressure application, Stage II was characterized by the initial contact between the inclined macroscopic ciliary array and the HEA hydrogel prior to buckling mode. As pressure increased, Stage III began with the transition from direct contact to a buckling mode between the HEA hydrogel and inclined macroscopic ciliary array, leading to an expanded EDL interfacial contact area; in Stage IV, the inclined macroscopic ciliary array collapsed completely, aligning its long axis parallel to the HEA hydrogel plane. During this process, PDMS acquired a net negative charge due to its inherent electronegativity, and the charged PDMS surface attracted counterions in the aqueous medium via Coulombic interactions to establish the EDL. Upon pressure release, the upward movement of the HEA hydrogel-coated top ITO electrode exposed unshielded charges on the PDMS surface, inducing opposite charges in the lower ITO electrode and generating a transient current flow from the upper to lower electrode, which ceased when the upper electrode halted. Throughout the cycle, the EDL capacitance is dynamically modulated by changes in the hydrogel PDMS contact area enabling real time linear conversion of pressure signals into electrical output.

To further validate the design rationale, PDMS inclined macroscopic ciliary array with varied tilt angles were fabricated as tribonegative dielectric layers and paired with positively charged nylon in contact-separation mode. Experimental results (Figure 1e) showed the triboelectric output peaked at 70 degrees, matching theoretical predictions. Systematic optimization of cilia geometry on standardized PDMS substrates revealed that a length of 0.4 cm minimized mechanical coupling interference, a diameter of 0.1 cm maximized sensitivity, and a spacing of 0.05 cm optimized contact area (Figure S3, Supporting Information). The curved cilia design amplified effective contact surface under load, increasing charge density and output. COMSOL simulations further confirmed the angular dependence of the output signal (Figure 1d). To reduce wear and improve mechanical robustness, a hydrogel was introduced as the tribopositive dielectric layer, balancing interfacial energy and durability. Contact-separation tests between hydrogel and PDMS inclined macroscopic ciliary array also showed maximum output at 70 degrees, validating the universal applicability of the golden ratio–guided design (Figure 1f).

2.2. Performance Optimization of BOIS

To explore the impact of these features on BOIS, we fabricated a series of hydrogel variants for comparative analysis. Building on this, the introduction of iontronic mechanisms, leveraging the mobile ions within the hydrogel matrix, has been shown in Wang et al. studies to further improve sensing performance by increasing interfacial capacitance and enabling more sensitive pressure responses. To examining the intrinsic material properties, we also integrated iontronic effects into selected hydrogel configurations to investigate their synergistic contributions to pressure sensing enhancement. Hydrogels are composed of a network of cross-linked polymers expanded by water. Due to their soft and deformable properties, they can closely adhere to the contact surface of the dielectric layer. Their intrinsic compliance allows for seamless contact with macroscopic structures, while the presence of surface free water layers promotes intimate interaction at the microscale. These features together lead to a significant increase in the effective contact area at the dielectric interface, which is critical for enhancing BOIS performance. Based on these characteristics, we designed and fabricated a series of hydrogel for comparative evaluation (**Figure 2a**).

The gelation of the HEA hydrogel relied on chemical crosslinking via free radical polymerization, forming a 3D polymer network (Figure S4a, Supporting Information). Under identical pressures, contact-separation tests between PDMS inclined macroscopic ciliary array and different hydrogels revealed that the HEA hydrogel generated optimal sensing signals (Figures 2b; S4b, Supporting Information), with its superior signal intensity enhancing noise immunity, sensitivity, and precision. Based on the binding strength and phase change behavior, water molecules in hydrogels can be classified into three categories, including strongly bound water (bound water), weakly bound water (intermediate water), and non-bound water (free water).[51] To demonstrate the correlation between the differences in output characteristics of various hydrogels and their water content, under the same conditions (store under conditions of 25 °C temperature and 17% relative humidity), we tested the water retention rates of different hydrogels. The experimental results showed that the mass retention rates of the hydrogels were comparable (Figure S4c, Supporting Information), indicating that the variations in electrical output were primarily attributed to differences in water states and ionic compositions rather than total water content. Parameter optimization of hydrogel structures demonstrated significant correlations between output characteristics and hydrogel parameters (Figure S5, Supporting Information). When HEA in contact-separation with PDMS, increasing hydrogel thickness from 1 to 3 mm elevated capacitance variation rates due to improved interfacial charge separation efficiency. Notably, varying crosslinker concentrations (1%–5%) caused less than 5% signal variability, indicating minimal dependence of the output signal on the crosslinking density. Systematic stress-strain testing identified a 3% crosslinker concentration combined with 1 mm thickness as optimal, balancing high sensitivity with mechanical adaptability to meet deformation compatibility requirements for flexible sensors monitoring multidirectional human joint motions. Finally, we confirmed that BOIS exhibits stable response capabilities under continuous pressure at different frequencies (Figure S6, Supporting Information). Its output voltage characteristics are significantly influenced by the contact-separation frequency of the TENG, a complex effect stemming from the coupled working mechanism of triboelectric charging and electrostatic induction that underlies TENG operation.

To validate the performance enhancement effect of the inclined macroscopic ciliary array on the BOIS, this study systematically compared it against a control system constructed from

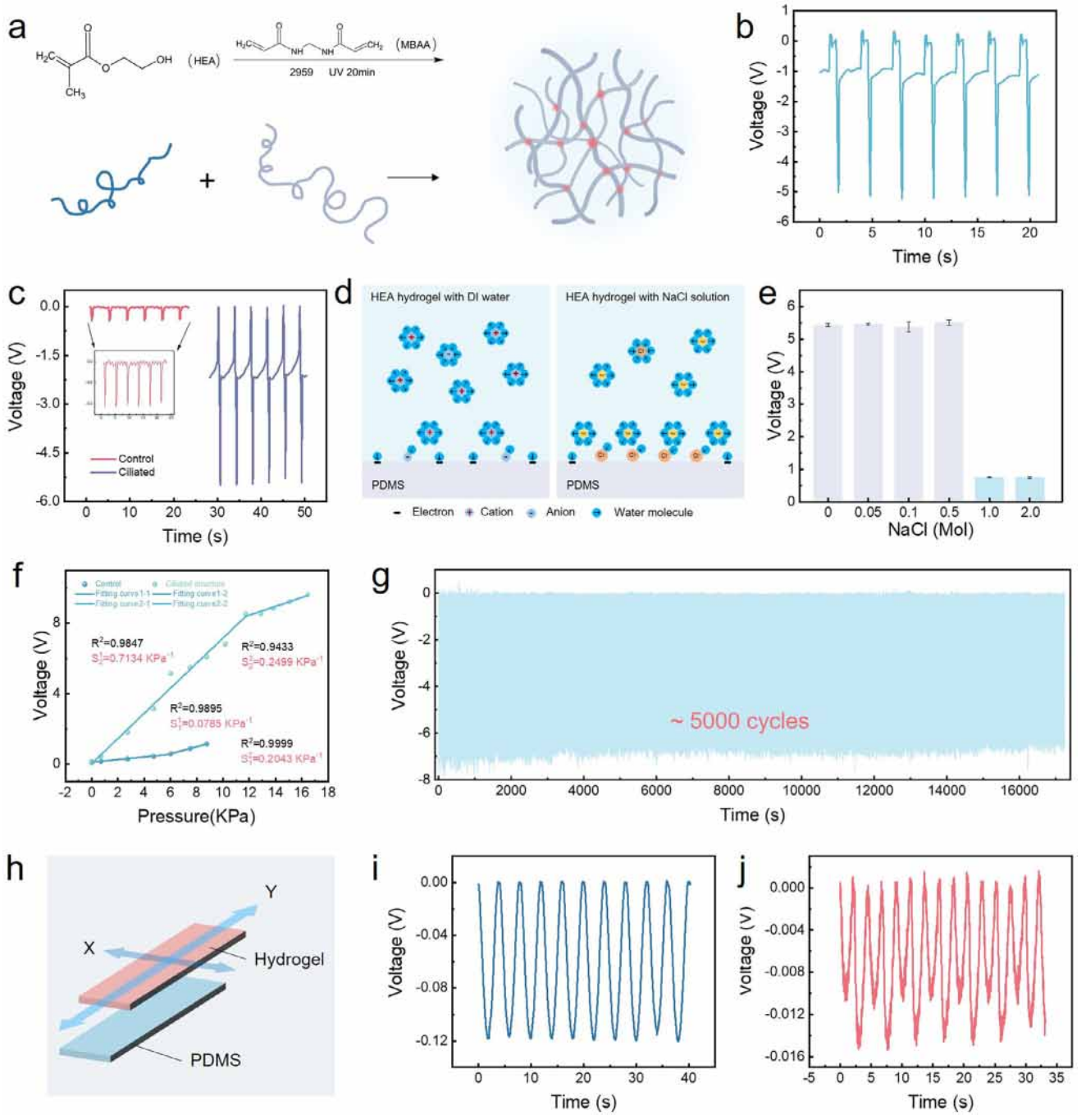

Figure 2. Analysis of the working principle and sensing performance of BOIS. a) Synthesis process of HEA hydrogel. b) Sensing signals of the device with inclined macroscopic ciliary array. c) Comparison of sensing performance between the device with inclined macroscopic ciliary array and the control system. d) Schematic diagram of the EDL at the hydrogel-PDMS interface. e) Comparison of sensing signals at different salt concentrations. f) Signal responses of the device with inclined macroscopic ciliary array and the control system under different pressures. g) Long-term stability test of the sensor with over 5000 loading/unloading cycles at 7 kPa. (h) Simplified omnidirectional force model. i,j) Under the same along the X axis and Y axis orthogonal lateral force, records in different directions to different peak voltage.

standardized PDMS substrates. Experimental data (Figure 2c) demonstrated that under identical pressure loading conditions, the device with the inclined macroscopic ciliary array exhibited a 12-fold enhancement in output signal amplitude compared to the control group (planar PDMS). This performance improvement originated from the array structure's optimization of interfacial charge transfer efficiency: the dynamic EDL-based BOIS could be equivalently modeled as a series capacitor circuit (Figure S7, Supporting Information), where the top electrode and charged hydrogel surface formed a fixed capacitance C_1, the EDL capacitance

C_2 at the PDMS-hydrogel interface dynamically varied with mechanical deformation, and the EDL capacitance C_3 at the PDMS-bottom electrode interface remained relatively stable. When mechanical motion disrupted the charge equilibrium of the EDL system, the inclined macroscopic ciliary array significantly amplified the induced charge density between electrodes by increasing the effective contact area, driving higher sensing signals in the external circuit. To thoroughly validate this mechanism, we performed "phase analysis" of the hydrogel-PDMS interface via electrochemical impedance spectroscopy (EIS). The results further revealed the patterns of resistance and capacitance changes during the interfacial process (Figure S8, Supporting Information). Furthermore, the sensor demonstrated stable operation under varying humidity conditions, confirming the device's universality across diverse environments.

To elucidate the iontronic enhancement mechanism in BOIS, charge transfer dynamics at the hydrogel-PDMS interface was systematically investigated by modulating the ionic concentration in the HEA hydrogel. When the HEA hydrogel was swelled by deionized water, the PDMS surface formed a stable charged interface through electron transfer mechanisms due to the H^+ ions present in the system (the hydrogel precursor solution was acidic, as shown in Figure S9, Supporting Information). As shown in Figure 2d, low-concentration NaCl (< 0.1 M) introduced negligible screening effects, allowing efficient ion-electron coupling at the interface. However, at higher concentrations (>0.5 M), excess free ions compressed the EDL, significantly suppressing interfacial electron transfer and resulting in a marked reduction in triboelectric output (Figure 2e). This trend was consistently observed with PAAM hydrogels (Figure S10, Supporting Information), corroborating "wo-step mechanism" describing charge regulation at liquid-dielectric boundaries. Further analysis using HEA-AA copolymer hydrogels revealed that the increased polarity of acrylic acid moieties altered interfacial hydration and weakened effective charge separation, leading to reduced signal intensities compared to pure HEA (Figure S11, Supporting Information). These results demonstrate that the introduction of iontronic EDL mechanisms not only enhances interfacial charge modulation but also provides a tunable strategy for optimizing pressure sensing performance through ionic composition and polymer polarity engineering.[52–54]

2.3. Characterization of BOIS

The introduction of inclined macroscopic ciliary array significantly influenced the dynamic response characteristics of the hydrogel and PDMS contact separation sensor, enabling synergistic enhancement of both sensitivity and detection range through the formation of multistage pressure responsive domains. As shown in the experimental results (Figure 2f), the inclined macroscopic ciliary array facilitated strain amplification through hierarchical buckling deformation modes under low pressure conditions (P < 12 kPa), resulting in a sensitivity of 0.7134 kPa^{-1} and demonstrating a strong linear correlation between output signal and applied pressure (R^2 = 0.9847). When pressure exceeded the critical threshold (P >12 kPa), the inclined macroscopic ciliary array transitioned to full compression, where the slowed contact area expansion reduced sensitivity to 0.2499 kPa^{-1}, accompanied by attenuated dynamic EDL capacitance variation rates. This pressure responsive dual-mode behavior distinguishes our design from planar PDMS sensors, which typically lack both low-pressure amplification and high-pressure tolerance. The inclined macroscopic ciliary array introduces controlled mechanical nonlinearity and stress distribution gradients, enabling enhanced sensitivity in the low-pressure region while expanding the upper detection limit. In comparison with state-of-the-art pressure sensors based on gel-dielectric contact-separation mechanisms, the BOIS demonstrates markedly improved sensitivity and a broader working range. Moreover, unlike conventional self-powered sensors that are typically limited to single-axis detection (Table S1, Supporting Information), BOIS enables omnidirectional force vector analysis due to the spatially oriented ciliary array, offering a distinct advantage for multidimensional tactile sensing.[53,55,56] Following silicone encapsulation, the device exhibited exceptional cyclic stability under periodic mechanical loading (frequency: 0.4 s^{-1}, pressure: 7 kPa). After 7000-cycle dynamic fatigue testing, the hydrogel-PDMS contact-separation output showed negligible signal decay (Figure 2g), a stability attributed to the encapsulation layer effectively suppressing hydrogel dehydration caused by ambient humidity fluctuations, ensuring long-term operational reliability.

Furthermore, the inclined macroscopic ciliary array architecture enabled the integration of classical contact and sliding operational modes within a single triboelectric framework, thereby achieving simultaneous detection of normal pressure and tangential friction forces. This design not only facilitated BOIS miniaturization but also endowed the system with dual-mode self-powered sensing capability, significantly broadening its applicability in omnidirectional tactile interfaces. In sliding mode, lateral mechanical stimuli induced surface parallel displacement between the hydrogel and PDMS layers, resulting in the generation of triboelectric charges due to interfacial electron affinity differences (Figure S12, Supporting Information). This lateral polarization drove electron flow between the top and bottom ITO electrodes to neutralize the triboelectric potential gradient, enabling directional sliding signal output. A simplified omnidirectional model (Figure 2h) incorporating a rectangular layout exhibited clear anisotropy in triboelectric output when subjected to identical lateral forces along orthogonal X and Y axes, with distinct peak voltages recorded in each direction (Figure 2i,j). This directional resolution confirms the ability of the BOIS to distinguish vector components of external shear stimuli. The experiment (Figure S13, Supporting Information) further systematically provided quantitative data on tangential forces from different angles, highlighting its outstanding performance in direction recognition and vector analysis. By integrating vertical contact-separation detection with a spatially oriented architecture, the system achieves full-field omnidirectional mechanical perception, including pressure, shear, and sliding, closely emulating natural tactile processes such as slip sensing. This capability provides high-fidelity force vector resolution, addressing a critical limitation of conventional planar or single-axis self-powered sensors, and enabling advanced applications in dexterous robotic manipulation, prosthetic haptic feedback, and adaptive HMIs.

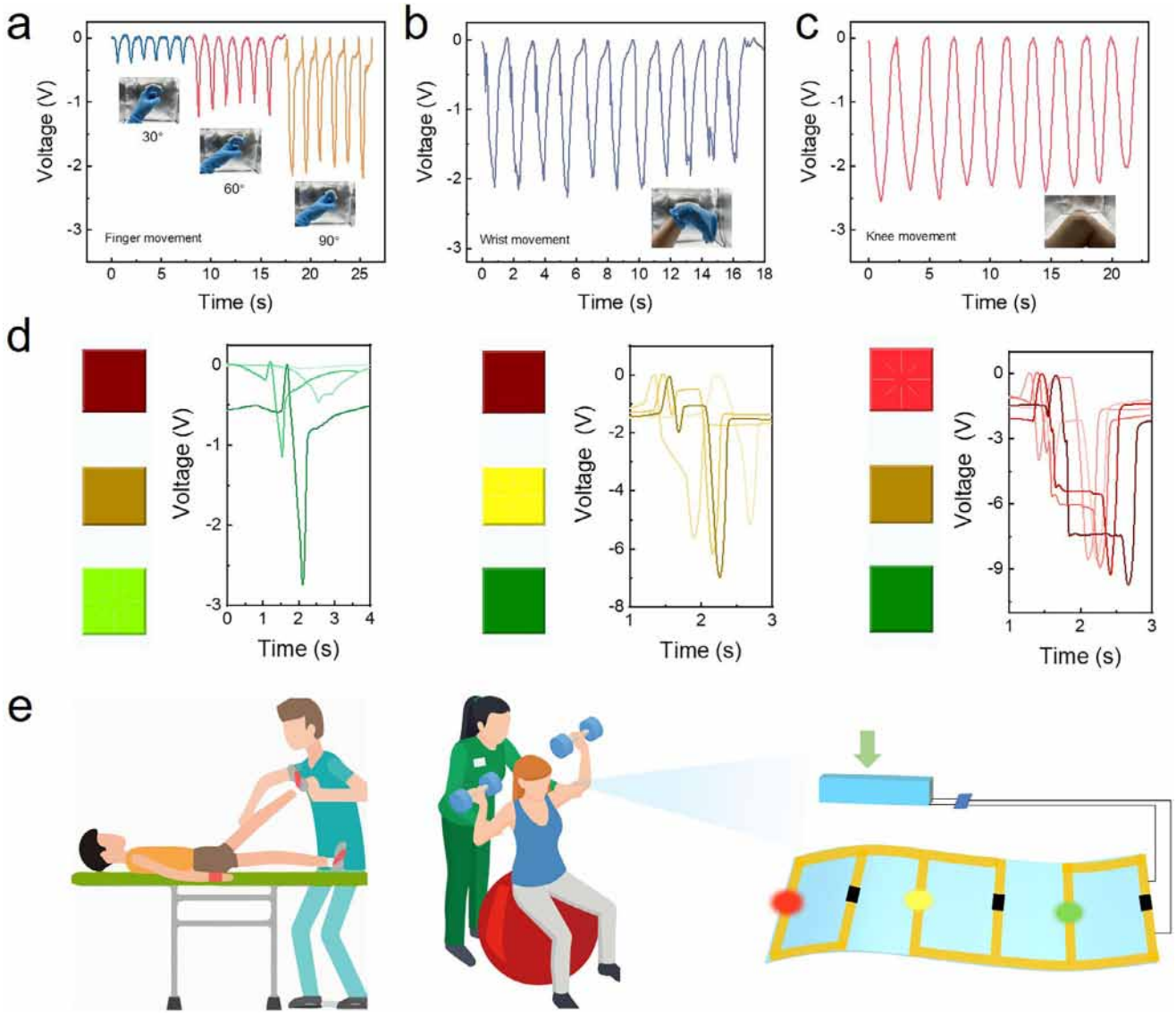

Figure 3. BOIS are used to detect different external stimuli demonstrations. a–c) Sensing signals change with the bending of fingers, wrists, and knees. d) Visual color feedback interface under different forces. e) Vision diagram of the BOIS used to assist in hand rehabilitation training.

2.4. Multimodal Applications of BOIS

Owing to its high sensitivity to both compressive and tensile deformations, the BOIS demonstrated robust performance in monitoring complex human motions, including finger bending, wrist articulation, and knee flexion. Integrated onto skin surfaces using medical adhesive tape, the sensor provided real-time, self-powered voltage outputs without external power modules, offering a significant advantage over conventional active pressure sensors. As shown in **Figure** 3a, voltage amplitudes increased proportionally with finger flexion angles (30°, 60°, and 90°), confirming its capacity for angle-resolved biomechanical monitoring in HMI applications. When deployed on wrist and knee joints (Figure 3b,c), the BOIS exhibited stable output under high-strain dynamic conditions, maintaining signal fidelity over repeated cycles without interfacial degradation. These results validated its mechanical robustness and charge retention under complex deformation, highlighting its potential for continuous wearable health monitoring and interactive robotics.

To enhance functionality, a self-powered visual feedback system was developed using LabVIEW to convert pressure signals into real-time, color-coded visual indicators (Figure 3d). Defined voltage thresholds triggered specific color responses: green for mild pressure ($0 < V < 3$ V), yellow for moderate ($3 < V < 8$ V), and red for high stress ($V > 8$ V). Reproducible visual outputs were obtained under cyclic force inputs, demonstrating system reliability. Furthermore, by integrating rectified sensor outputs with a series-resistor-parallel-LED circuit, a discrete LED feedback platform was established for rehabilitation applications (Figure 3e). The voltage division mechanism enabled differential LED illumination correlated with stress levels, providing intuitive guidance for patients to modulate exertion during therapeutic

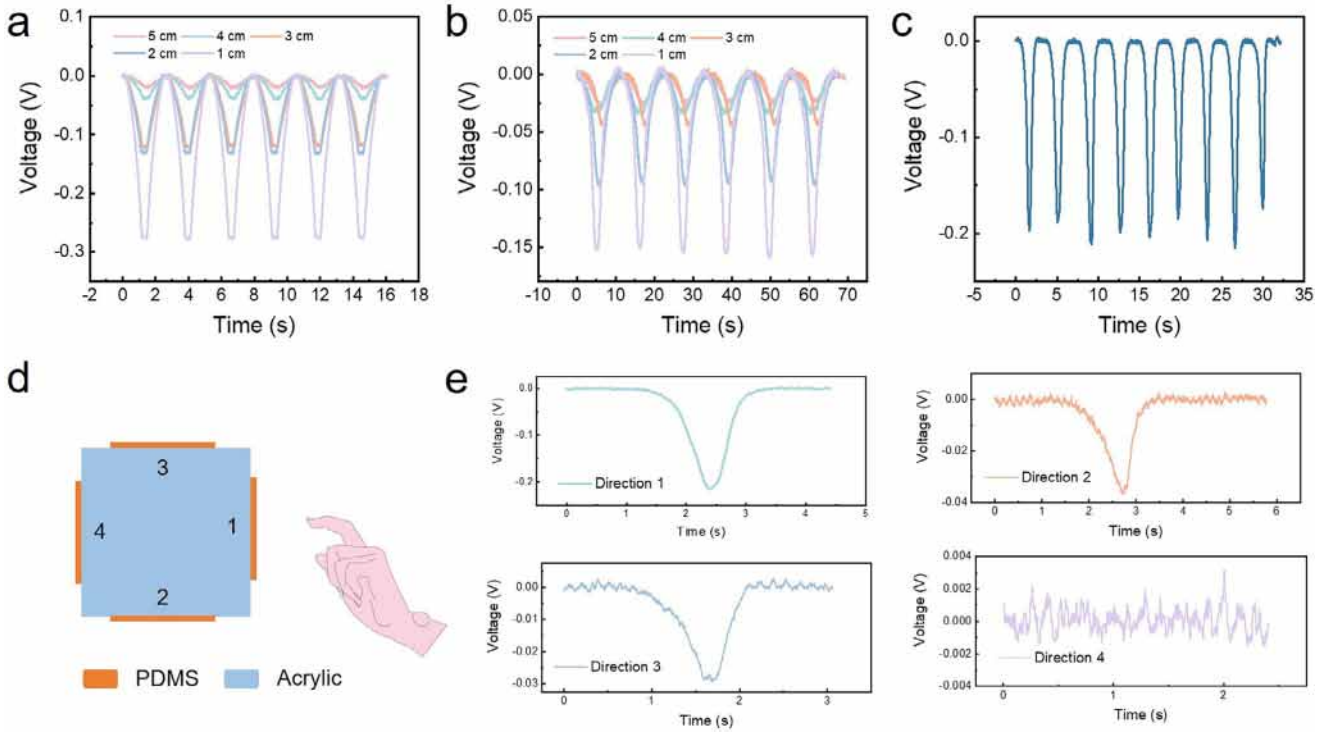

Figure 4. The non-contact sensing capability of the PDMS inclined macroscopic ciliary array. a) Signal amplitudes of vertical approach of nylon-PDMS at different distances. b) Signal amplitudes of lateral sliding of nylon-PDMS at different distances. c) Sensing signal of finger approaching 3 cm from PDMS. d) Schematic diagram of a 3D sensing network structure composed of a four-element PDMS cilia array. e) Sensing signals of different channels after finger approach.

exercises. This system offers a promising strategy for real-time visual feedback in personalized rehabilitation and adaptive training.

Beyond conventional contact-based pressure and shear sensing, the inclined macroscopic ciliary array architecture imparts intrinsic non-contact sensing capabilities via tribo-induced electrostatic induction.[57,58] As illustrated in Figure S14 (Supporting Information), this mechanism relied on pre-established surface charges generated through initial contact separation cycles between the PDMS inclined macroscopic ciliary array and a positively charged nylon film. The resulting surface potential on the PDMS enabled dynamic electrostatic interactions during subsequent approach or sliding of the nylon film without physical contact. When the nylon approached the PDMS surface, the resulting spatial charge gradient induced electron migration from the electrode to the ground, generating a detectable voltage signal. As the nylon retracted, the induced electrostatic field diminished, prompting reverse electron flow to restore electrostatic equilibrium. This contactless sensing cycle, governed entirely by distance-dependent electrostatic coupling, enabled real-time detection of proximity stimuli. To validate this behavior, a nylon film (1 cm × 5 cm) was mounted on a programmable linear motor, allowing precise control of its displacement relative to the PDMS cilia surface. Output measurements under both vertical approach and lateral sliding modes revealed a consistent inverse linear correlation between signal amplitude and separation distance (**Figure** 4a,b), in agreement with theoretical models of electrostatic field attenuation in open triboelectric systems. The integration of inclined macroscopic ciliary array structures was critical for enhancing noncontact responsiveness. Their high aspect ratio and spatial orientation increased the effective electrostatic interaction area, amplifying induced surface potential changes and improving signal resolution under weak field conditions. To systematically validate the universality of this sensing mechanism across diverse material systems, the study expanded beyond nylon film testing to include materials with varying electronegativity (including aluminum foil, FEP film, PI film, and PTFE film). It systematically investigated their dynamic electrostatic interactions with a PDMS inclined macro-cilia array under non-contact conditions (spacing 1–5 cm). Experimental results demonstrate (Figure S15, Supporting Information) that all tested materials generate significant and reproducible non-contact electrical signals, whose intensity exhibits a regular attenuation with increasing distance. This further confirms the broad applicability of this non-contact sensing mechanism across diverse material types.

To further demonstrate the non-contact sensing capability, approach experiments using a human finger at a distance of 3 cm were conducted. As shown in Figure 4c, a clear voltage signal was generated when the finger entered the electrostatic induction range of the PDMS inclined macroscopic ciliary array, confirming its effectiveness in air-gap sensing. To enable spatial perception beyond single-point detection, a 3D sensing array was constructed using four PDMS inclined macroscopic ciliary array units arranged orthogonally on the surfaces of an acrylic cube (6 cm × 6 cm × 6 cm), as shown in Figure 4d. Each unit had

directionally aligned cilia structures labeled as Direction 1 to Direction 4. When a finger approached from Direction 1, only the corresponding unit produced a strong voltage signal (Figure 4e), while adjacent units showed weaker responses. This gradient output pattern resulted from the asymmetric distribution of the electrostatic field and the orientation-specific response of the inclined macroscopic ciliary array, enabling accurate identification of the approach direction. This spatially resolved non-contact sensing approach provides enhanced direction discrimination and broadens the application potential of the system in areas such as motion tracking and intelligent interfaces.

To quantitatively evaluate the impact of humidity on sensor performance, we conducted non-contact sensing tests under different relative humidity conditions (20%, 50%, and 90%). In the experiment, a nylon film was fixed at a specific distance near the PDMS inclined macroscopic ciliary array. As shown in Figure S16 (Supporting Information), the sensor output signal exhibited minimal variation across a wide humidity range, demonstrating excellent stability. This stability stems from the mechanism of signal generation in non-contact mode: the signal primarily relies on the electrostatic field formed on the pre-charged PDMS surface. As an excellent dielectric material, PDMS deeply confines surface charges within bulk trap energy levels, exhibiting extremely long charge relaxation times. Changes in ambient humidity primarily affect the adsorbed water film several molecular layers thick on the material surface, making it difficult to penetrate the PDMS bulk and alter the distribution of trapped charges. This ensures the stability of the electrostatic field. Furthermore, the inclined macroscopic ciliary array structure itself significantly enhances non-contact sensing sensitivity compared to planar PDMS films. The high aspect ratio and spatial orientation of the cilia generate stronger anisotropic electric field gradients, enabling the excitation of more robust sensing signals when external objects approach. To validate this advantage, a 3D sensing array was constructed by orthogonally arranging four PDMS inclined macro-cilia array units on an acrylic cube surface. A finger was then approached from a specific direction (Direction 1). Compared to the flat PDMS film, the inclined macroscopic ciliary array not only exhibited higher signal intensity but also demonstrated clear directional recognition capability.

3. Conclusion

In summary, we developed a BOIS that integrates triboelectric coupling with a Fibonacci spiral guided, 70° inclined macroscopic ciliary array to achieve comprehensive omnidirectional mechanical sensing. Inspired by the spatial encoding mechanism of cochlear cilia, this tilt-optimized architecture facilitates hierarchical buckling deformation, resulting in linear sensitivity of 0.7134 kPa^{-1}. The incorporation of a hydrogel/PDMS interface introduces dynamic EDL modulation during asymmetric contact-separation cycles, enhancing signal output and responsiveness. This combination of bioinspired structural geometry and triboiontronic effects enables simultaneous contact and non-contact sensing with real-time omnidirectional force detection and vector analysis capabilities, overcoming the limitations of uniaxial sensing prevalent in conventional devices. The system achieves full-field omnidirectional force perception, including pressure, shear, and slip, closely emulating natural tactile sensing and delivering essential multidirectional feedback for advanced applications such as robotic manipulation, prosthetic interfaces, and adaptive HMI. Its scalable one-step molding process enables precise replication of complex structures and seamless integration into flexible electronics. Demonstrated use cases in motion tracking and joint monitoring highlight its potential in electronic skin, wearable HMIs, and rehabilitation technologies. Collectively, this work establishes a robust and scalable platform for next-generation self-powered tactile sensors capable of operating under complex, multidimensional mechanical stimuli.

4. Experimental Section

Materials: PDMS (Sylgard 184) was bought from Dow Corning Co., Ltd. Indium-tin oxide (ITO)-coated poly (ethylene terephthalate) (PET) sheets (125μm-thick) were bought from Huanan Xiangcheng Co., Ltd. Acrylamide (AAM), N,N'-Methylenebisacrylamide (MBAA) were bought Shanghai Macklin Biochemical Co., Ltd. 2-Hydroxyethyl acrylate (HEA), Acrylic acid (AA), Agar, Sodium chloride (NaCl) were bought from Shanghai Aladdin Biochemical Technology Co., Ltd. 2-Hydroxy-1-[4-(2-hydroxyethoxy)phenyl]-2-methyl-1-propanone (I2959) was bought from Suzhou Suosen New Materials Technology Co., LTD.

Preparation of PDMS Inclined Macroscopic Ciliary Array: Custom negative molds with different inclined channels were fabricated using high-resolution stereoscopic lithography 3D printing with polyvinyl alcohol (PVA) as sacrifice material. The PDMS precursor (Base material and curing agent mixed in a 10:1 ratio) was cast into the mold, degassed, and thermally cured at 60 °C for 4 h to form a flexible elastomeric matrix. Subsequent immersion in deionized water selectively dissolved the embedded PVA, yielding a freestanding PDMS membrane with uniformly aligned, inclined macroscopic cilia arrays. The parameters of PDMS inclined ciliary array are described in this paper. The base size of PDMS under inclined ciliary array is 50 mm × 10 mm × 1 mm. Used as a control group of planar PDMS size 50 mm × 10 mm × 1 mm.

Preparation of Hydrogels: 1) 750 mg of AAM, 7.5 mg of MBAA, and 50 mg of I2959 were added to 5 mL of deionized water, and the drugs were completely dissolved by stirring and sonication. 2) 0.7 mL HEA, 7.5 mg MBAA, and 50 mg I2959 were added to 5 mL of deionized water, and the drug was completely dissolved by stirring and sonication. 3) 0.4 mL HEA, 0.4 mL AA, 7.5 mg MBAA, and 50 mg I2959 were added to 5 mL of deionized water, and the drugs were completely dissolved by stirring and sonication. The above clarified solution was added to a 3D printed PET template (50 mm × 10 mm × 1 mm), covered with a glass sheet and guaranteed to be free of bubbles. Finally, the corresponding hydrogel was obtained after 20 min of ultraviolet (UV) light irradiation. 4) 5wt.% Agar permanent solution was prepared and heated to 100 °C to completely dissolve the Agar. The above clarified solution was added to the PET template using 3D printing and cooled to room temperature to obtain the Agar gel.

Preparation of Hydrogels with Different Ionic Concentrations: Different concentrations of NaCl (0, 0.05, 0.1, 0.5, 1, and 2 M, respectively) were dissolved into the above clarified solution. A 15 min ultrasonic water bath is used to remove bubbles from the solution. The above clarified solution was added to a 3D printed PET template, covered with a glass sheet and guaranteed to be free of bubbles. Finally, hydrogels with different ion concentrations were obtained after 20 min of UV irradiation.

Electric Measurement: A linear motor (LinMotS01-72/500) was used for contact separation of hydrogel and PDMS. The digital push-pull force gauge (DF-500) is used to measure the pressure exerted on the sensor. The open-circuit voltage of BOIS was measured using a programmable electrostatic voltmeter (Keithley 6514). To test the basic output performance of BOIS, a programmable electrostatic voltmeter (Keithley 6514) was directly connected to a synchronous data acquisition card (National Instruments 6346) to measure multi-channel voltage signals. A multi-channel data acquisition program developed on the LabVIEW platform is used for data acquisition, processing, and storage.

Consent Statements: This study involved experiments using wearable sensor technology with human participants, all of whom provided written informed consent.

Supporting Information

Supporting Information is available from the Wiley Online Library or from the author.

Acknowledgements

This work was supported by the National Natural Science Foundation of China (grant number 22479016).

Conflict of Interest

The authors declare no conflict of interest.

Author Contributions

Z.Z., Y.D., and Y.Z. contributed equally to this work. D.W. and Z.L.W. proposed the idea and the project. D.W. supervised the whole project. Z.K.Z. designed all the experiments and carried out the experiments in this paper, and analyzed the corresponding data. Y.D. assisted in experimental testing and completed the finite element theoretical analysis model. Y.Y.Z. finished the theoretical modeling of COMSOL. J.F. helped to realize the application of human-machine interaction. Y.W.O.Y. participated in the experimental characterization and analysis. All the authors discussed the results and commented on the manuscript. D.W. and Z.K.Z. wrote this paper.

Data Availability Statement

The data that support the findings of this study are available from the corresponding author upon reasonable request.

Keywords

no-contact sensing, omnidirectional iontronic sensors, pressure sensors, triboelectric nanogenerators

Received: August 20, 2025
Revised: November 7, 2025
Published online: January 20, 2026

[1] S. Lee, S. Franklin, F. A. Hassani, T. Yokota, M. O. G. Nayeem, Y. Wang, R. Leib, G. Cheng, D. W. Franklin, T. Someya, *Science* **2020**, *370*, 966.
[2] Y.-C. Huang, Y. Liu, C. Ma, H.-C. Cheng, Q. He, H. Wu, C. Wang, C.-Y. Lin, Y. Huang, X. Duan, *Nat Electron* **2020**, *3*, 59.
[3] S. Min, J. An, J. H. Lee, J. H. Kim, D. J. Joe, S. H. Eom, C. D. Yoo, H.-S. Ahn, J.-Y. Hwang, S. Xu, J. A. Rogers, K. J. Lee, *Nat. Rev. Cardiol.* **2025**, *22*, 629.
[4] W. Li, X. Li, X. Xiao, F. Manshaii, X. Luo, G. Chen, W. Li, G. Xie, H. Tai, Y. Jiang, Y. Su, J. Chen, *Adv. Mater.* **2025**, *37*, 07169.
[5] J. Xu, C. Duan, X. Wan, Z. Che, X. Zhao, Y. Zhou, Y. Song, J. Yin, T. Tat, S. Li, J. Chen, *Nat. Electron.* **2025**, *8*, 709.
[6] K. Nan, S. Babaee, W. W. Chan, J. L. P. Kuosmanen, V. R. Feig, Y. Luo, S. S. Srinivasan, C. M. Patterson, A. M. Jebran, G. Traverso, *Nat. Biomed. Eng.* **2022**, *6*, 1092.
[7] R. Chen, T. Luo, J. Wang, R. Wang, C. Zhang, Y. Xie, L. Qin, H. Yao, W. Zhou, *Nat. Commun.* **2023**, *14*, 6641.
[8] Y. Zhi, H. Zhang, L. Zhang, Q. Li, X. Kuang, W. Wu, Q. Zhou, P. Li, W. Li, H. Zhang, *Adv. Fiber Mater.* **2025**, *7*, 541.
[9] Y. Cheng, Y. Zhan, F. Guan, J. Shi, J. Wang, Y. Sun, M. Zubair, C. Yu, C. F. Guo, *Natl. Sci. Rev.* **2024**, *11*, nwae050.
[10] J. Shi, S. Xie, Z. Liu, M. Cai, C. F. Guo, *Natl. Sci. Rev.* **2024**, *11*, nwae351.
[11] J. Song, R. Yang, J. Shi, X. Chen, S. Xie, Z. Liao, R. Zou, Y. Feng, T. T. Ye, C. F. Guo, *Sci. Adv.* **2025**, *11*, adu6086.
[12] Z. Wang, Y. Tai, Z. Ye, J. Nam, Y. Yin, *Adv. Funct. Mater.* **2024**, *34*, 2410358.
[13] Z.-X. Huang, L.-W. Li, Y.-Z. Huang, W.-X. Rao, H.-W. Jiang, J. Wang, H.-H. Zhang, H.-Z. He, J.-P. Qu, *Nat. Commun.* **2024**, *15*, 819.
[14] D. B. Kim, J. Han, S. M. Sung, M. S. Kim, B. K. Choi, S. J. Park, H. R. Hong, H. J. Choi, B. K. Kim, C. H. Park, J. H. Paik, J.-S. Lee, Y. S. Cho, *npj Flex Electron* **2022**, *6*, 69.
[15] Z. Nie, J. W. Kwak, M. Han, J. A. Rogers, *Adv. Mater.* **2024**, *36*, 2205609.
[16] H. Niu, H. Li, N. Li, H. Niu, S. Gao, W. Yue, Y. Li, *Appl. Phys. Rev.* **2025**, *12*, 011319.
[17] K. Meng, X. Xiao, W. Wei, G. Chen, A. Nashalian, S. Shen, X. Xiao, J. Chen, *Adv. Mater.* **2022**, *34*, 2109357.
[18] Y. Lu, H. Tian, J. Cheng, F. Zhu, B. Liu, S. Wei, L. Ji, Z. L. Wang, *Nat. Commun.* **2022**, *13*, 1401.
[19] T. Bhatta, S. Sharma, K. Shrestha, Y. Shin, S. Seonu, S. Lee, D. Kim, Md. Sharifuzzaman, S. S. Rana, J. Y. Park, *Adv. Funct. Mater.* **2022**, *32*, 2202145.
[20] J. Jiang, X. Song, Y. Qi, X. Tao, Z. Zheng, Q. Huang, *Adv. Fiber Mater.* **2025**, *7*, 894.
[21] Y. Liu, J. Wang, T. Liu, Z. Wei, B. Luo, M. Chi, S. Zhang, C. Cai, C. Gao, T. Zhao, S. Wang, S. Nie, *Nat. Commun.* **2025**, *16*, 383.
[22] M. Guo, Y. Xia, J. Liu, Y. Zhang, M. Li, X. Wang, *Adv. Funct. Mater.* **2025**, *35*, 2419209.
[23] O. Verners, A. Šutka, I. Arief, A. Das, K. Mālnieks, J. Lungevičs, *Mater. Sci. Eng., B* **2025**, *317*, 118140.
[24] S. Lee, J.-W. Park, *Nano Energy* **2022**, *101*, 107546.
[25] N. Bai, L. Wang, Y. Xue, Y. Wang, X. Hou, G. Li, Y. Zhang, M. Cai, L. Zhao, F. Guan, X. Wei, C. F. Guo, *ACS Nano* **2022**, *16*, 4338.
[26] T. Li, P. Pan, Z. Yang, J. Wei, X. Yang, J. Liu, J. Zhou, X. Zhang, G. Liu, *Adv. Mater. Technol.* **2022**, *7*, 2101135.
[27] C. K. Chung, K. H. Ke, *Appl. Surf. Sci.* **2020**, *508*, 145310.
[28] L. Wu, X. Li, J. Choi, Z.-J. Zhao, L. Qian, B. Yu, I. Park, *Adv. Funct. Mater.* **2024**, *34*, 2312370.
[29] P. Lu, L. Wang, P. Zhu, J. Huang, Y. Wang, N. Bai, Y. Wang, G. Li, J. Yang, K. Xie, J. Zhang, B. Yu, Y. Dai, C. F. Guo, *Sci. Bull.* **2021**, *66*, 1091.
[30] Y. Zhang, J. Yang, X. Hou, G. Li, L. Wang, N. Bai, M. Cai, L. Zhao, Y. Wang, J. Zhang, K. Chen, X. Wu, C. Yang, Y. Dai, Z. Zhang, C. F. Guo, *Nat. Commun.* **2022**, *13*, 1317.
[31] H. Niu, H. Li, S. Gao, Y. Li, X. Wei, Y. Chen, W. Yue, W. Zhou, G. Shen, *Adv. Mater.* **2022**, *34*, 2202622.
[32] K. K. Meena, I. Arief, A. K. Ghosh, A. Knapp, M. Nitschke, A. Fery, A. Das, *Small* **2025**, *21*, 2502767.
[33] L. Zhao, Q. Zheng, H. Ouyang, H. Li, L. Yan, B. Shi, Z. Li, *Nano Energy* **2016**, *28*, 172.
[34] W.-G. Kim, I.-W. Tcho, D. Kim, S.-B. Jeon, S.-J. Park, M.-L. Seol, Y.-K. Choi, *Nano Energy* **2016**, *27*, 306.
[35] S. Kang, J. Lee, S. Lee, S. Kim, J.-K. Kim, H. Algadi, S. Al-Sayari, D.-E. Kim, D. Kim, T. Lee, *Adv. Electron. Mater.* **2016**, *2*, 1600356.
[36] S. Qin, P. Yang, Z. Liu, J. Hu, N. Li, L. Ding, X. Chen, *Nat. Commun.* **2024**, *15*, 10640.
[37] L. Robles, M. A. Ruggero, *Physiol. Rev.* **2001**, *81*, 1305.
[38] M. M. Mellado Lagarde, M. Drexl, V. A. Lukashkina, A. N. Lukashkin, I. J. Russell, *Nat. Neurosci.* **2008**, *11*, 746.

[39] S. Strauss, J. Lempe, P. Prusinkiewicz, M. Tsiantis, R. S. Smith, *New Phytologist* **2020**, *225*, 499.
[40] G. J. Mitchison, *Science* **1977**, *196*, 270.
[41] Y. Li, N. Bai, Y. Chang, Z. Liu, J. Liu, X. Li, W. Yang, H. Niu, W. Wang, L. Wang, W. Zhu, D. Chen, T. Pan, C. F. Guo, G. Shen, *Chem. Soc. Rev.* **2025**, *54*, 4651.
[42] X. Li, R. Li, S. Li, Z. L. Wang, D. Wei, *Nat. Commun.* **2024**, *15*, 6182.
[43] Y. Ouyang, X. Li, S. Li, P. Peng, F. Yang, Z. L. Wang, D. Wei, *Nano Energy* **2023**, *116*, 108796.
[44] X. Li, S. Li, X. Guo, J. Shao, Z. L. Wang, D. Wei, *Matter* **2023**, *6*, 3912.
[45] Z. L. Wang, A. C. Wang, *Mater. Today* **2019**, *30*, 34.
[46] J. Chen, Y. Wang, B. Wang, Z. Liu, W. Chen, Z. Chen, N. Zhang, C. Gui, *Nano Energy* **2025**, *139*, 110922.
[47] K. K. Meena, I. Arief, A. K. Ghosh, H. Liebscher, S. Hait, J. Nagel, G. Heinrich, A. Fery, A. Das, *Nano Energy* **2023**, *115*, 108707.
[48] H. Zhang, H. Chen, J.-H. Lee, E. Kim, K.-Y. Chan, H. Venkatesan, M. H. Adegun, O. G. Agbabiaka, X. Shen, Q. Zheng, J. Yang, J.-K. Kim, *Adv. Funct. Mater.* **2022**, *32*, 2208362.
[49] S. Kim, W. Cho, J. Hwang, J. Kim, *Nano Energy* **2023**, *107*, 108109.
[50] S. G. Wagner, *The Fibonacci Quarterly* **2007**, *45*, 247.
[51] Y. Yuan, Q. Zhang, S. Lin, J. Li, *Prog. Mater. Sci.* **2025**, *148*, 101378.
[52] Y. Ouyang, X. Li, S. Li, Z. L. Wang, D. Wei, *ACS Appl. Mater. Interfaces* **2024**, *16*, 18236.
[53] L. Jia, Z. H. Guo, L. Li, C. Pan, P. Zhang, F. Xu, X. Pu, Z. L. Wang, *ACS Nano* **2021**, *15*, 19651.
[54] X. Li, Y. Wei, X. Gao, Z. Zhang, Z. L. Wang, D. Wei, *Joule* **2025**, *9*, 101888.
[55] G. Zhao, Y. Zhang, N. Shi, Z. Liu, X. Zhang, M. Wu, C. Pan, H. Liu, L. Li, Z. L. Wang, *Nano Energy* **2019**, *59*, 302.
[56] K. Zhao, H. Lv, J. Meng, Z. Song, C. Meng, M. Liu, D. Zhang, *ACS Omega* **2022**, *7*, 18816.
[57] Y. Du, P. Shen, H. Liu, Y. Zhang, L. Jia, X. Pu, F. Yang, T. Ren, D. Chu, Z. Wang, D. Wei, *Sci. Adv.* **2024**, *10*, adp8681.
[58] J. Guo, Y. Du, Z. Wang, D. Wei, *J. Mater. Chem. A* **2025**, *13*, 8939.